Monthly Notices
of the
ROYAL ASTRONOMICAL SOCIETY

MNRAS **493,** 2229–2237 (2020)
Advance Access publication 2020 February 10

doi:10.1093/mnras/staa338

Observational signatures of gamma-rays from bright blazars and wakefield theory

N. E. Canac,[1] K. N. Abazajian ,[1★] T. Tajima,[1] T. Ebisuzaki[2] and S. Horiuchi [3]

[1]*Department of Physics and Astronomy, University of California, Irvine, CA 92697, USA*
[2]*RIKEN, 2-1 Hirosawa, Wako, Saitama, 351-0198, Japan*
[3]*Center for Neutrino Physics, Department of Physics, Virginia Tech, Blacksburg, VA 24061, USA*

Accepted 2020 January 31. Received 2020 January 31; in original form 2019 March 12

ABSTRACT

Gamma-ray observations have revealed strong variability in blazar luminosities in the gamma-ray band over time-scales as short as minutes. We show, for the first time, that the correlation of the spectrum with intensity is consistent with the behaviour of the luminosity variation of blazar spectral energy distributions (SEDs) along a blazar sequence for low synchrotron peak blazars. We show that the observational signatures of variability with flux are consistent with wakefield acceleration of electrons initiated by instabilities in the blazar accretion disc. This mechanism reproduces the observed time variations as short as 100 s. The wakefield mechanism also predicts a reduction of the electron spectral index with increased gamma-ray luminosity, which could be detected in higher energy observations well above the inverse Compton peak.

Key words: acceleration of particles – plasmas – galaxies: active – gamma-rays: galaxies.

1 INTRODUCTION

Bright gamma-ray emitting blazars have been detected to have variability in flux by a factor of 2 or more on time-scales from minutes to weeks (Aharonian 2007; Albert et al. 2007; Abdo et al. 2010a,d; Aleksic et al. 2011). This short-scale temporal variability has presented a strong challenge to jet emission models. The spectral indices are often also time variable, around the index of 2 or greater (Albert et al. 2007; Abdo et al. 2010a; Chen et al. 2013). Furthermore, an anticorrelation of the spectral index and the gamma-ray flux is also reported (Abdo et al. 2010a), which implies a connection to the underlying emission mechanism. The High Energy Stereoscopic System (H.E.S.S.) telescope has observed flares on time-scales of $\sim$200 s in very high energy (VHE) $>$ 100 GeV gamma-rays with peak fluxes at a factor of 2 above the average flux toward the blazar PKS 2155−304 (Aharonian 2007). The Major Atmospheric Gamma Imaging Cherenkov (MAGIC) telescope has seen flux variability by an order of magnitude over several minutes, with a hardening of the spectrum (corresponding to lower spectral index) with increasing flux (Albert et al. 2007). Similar variation is seen in PKS 1222+21 in VHE observations by MAGIC, with a potential smooth spectral connection to the GeV scale in observations by the Large Area Telescope of *Fermi Gamma-Ray Space Telescope* (*Fermi*-LAT; Aleksic et al. 2011).

The lack of a strong spectral break in the VHE gamma-rays has indicated that the jet emission mechanism must be outside of the broad-line emission region (BLR), i.e. away from the region's very high photon densities. From the temporal variability it can be inferred that the emission region must be very compact, of order $\sim 10^{14}$ cm from causality. To avoid the optical depth within the BLR, it has been hypothesized that there are small-scale regions embedded within a larger jet (e.g. Giannios, Uzdensky & Begelman 2009). Accommodating these phenomena in traditional jet emission models has proved so challenging, as to motivate new axion-like particles to allow for photon–axion mixing to potentially provide the temporal variability and spectral features (e.g. Tavecchio et al. 2012). Alternatively, studies have tied the time-scales optical variability with episodic emission in the magnetic field of the jet (Marscher et al. 2008; Edelson et al. 2013, 2014).

Fermi-LAT observations have revealed GeV gamma-ray signatures from the brightest blazars (Abdo et al. 2010a). Notably the gamma-ray observations from blazar AO 0235+164 and 3C 454.3 show similar properties such as:

(i) the photon index is around 2 or slightly above 2 in their respective lowest value;

(ii) the photon index varies rapidly from its lowest (around 2) to highest (around 2.8 or so) value over a period of several weeks;

(iii) the luminosity (flux) of the gamma-rays also varies rapidly over the same time period of several weeks, by as much as a factor of 5;

(iv) and, most importantly, the luminosity peak and the valley (hardening) of the photon index positively coincide. In other words, the time variations of the photon index and luminosity faithfully anticorrelate. This anticorrelation clearly persists regardless of dif-

---

[★] E-mail: kevork@uci.edu

Published by Oxford University Press on behalf of the Royal Astronomical Society

ferent periods from hundreds of seconds to months, demonstrating a remarkable universality in the phenomenon.

We show in this paper, for the first time, that the rapid variations of high-energy gamma emissions and the strong anticorrelation between the luminosity and photon index is consistent with a blazar spectral energy distribution (SED) sequence shift. We further show that the timing of the variations is consistent with magnetorotational episodic instabilities, recently studied in Mizuta et al. (2018). We show that the inherent acceleration mechanism may be probed by further analysis of the highest energy blazar spectra and their variability.

The above indication of the position away from the high-density region, the inferred compactness of the emission region, and the minute time-scale variabilities, all indicate a mechanism of the variability arising from high-energy electrons from more compact and robust energy conversion than can be provided by Fermi stochastic acceleration. The wakefield acceleration of electrons can provide such a viable mechanism with the properties that may fit and explain these features (Ebisuzaki & Tajima 2014a). When the magnetorotational instability (MRI) enhances magnetic fields in the inner accretion disc of the blazar (Balbus & Hawley 1991; Matsumoto & Tajima 1995) and episodically causes a large variability in matter accretion, this can severely disturb the base of the jets. These shock waves at the jet base, i.e. large amplitude Alfven waves, propagate along the jets, eventually mode convert themselves into intense relativistic electromagnetic (EM) pulses along the jets. These excitations of EM pulses are capable of giving rise to bow wakes, which accelerate electrons to high energies (only limited by their emissions of radiation; Ebisuzaki & Tajima 2014a). This process is prompt, energy efficient and robust, and known to hold a stiff energy power spectrum.

The additional features of blazar's observational phenomena include that high-energy gamma photon emissions are episodic: they contain very short time-scale structure within one burst, as well as longer evolution and much longer scale variability. Because of these features, we can relate the above observed properties to their physical origins. The central compact object black hole is the source of the energy of the burst, which is accompanied by an active accretion disc, which in turn spawns out a pair of (spiral) jets. Young objects of active galactic nuclei (AGN)/galactic systems provide active dynamical, rather than stochastic, and robust plasma and magnetic activities (as described in Tajima & Shibata 2002). The directionality of blazar and good robust conversion of gravitational energy of such a disc into the accretion and emission processes are required to be explained in any complete model. In order for such active and large energetic occurrence to happen, we surmise that 'collective' (as opposed to 'individual') forces convert energy of gravitation effectively and in a short matter of time. In prior work, it was shown that short-range collisional processes are likely too slow and non-dynamical, while the plasma's collective interaction is long ranged and far reached (Ebisuzaki & Tajima 2014a; Mizuta et al. 2018).

Our model for the gamma-ray variability from blazars is as follows (see also Ebisuzaki & Tajima 2014a): the gravitational energy in young accretion disc rotational motion is stored as magnetic energy build-up by the shear rotation of the disc via the MRI (Balbus & Hawley 1991). The build-up may be disrupted due to its explosive growth (Mizuta et al. 2018). This eruption of the magnetic fields in the disc accompanies disruptive episodic large accretion of disc matter toward the central object and its jets. Severe shaking of the base of the jets of AGN – jets accompanying spiral magnetic fields – causes severe Alfvenic shocks whose wavelength along the jet. This is determined by the size of the infalling accretion material (as in Mizuta et al. 2018). The shock wave propagation along the jets from their source converts modes of Alfven waves eventually into EM pulses, as the density and magnetic field strengths go down as they propagate, with its frequency preserved. This constitutes a spontaneously generated large-scale emission of wakefields, and gives rise to immense wakefield acceleration of leptonic and hadronic cosmic rays. The sum total of these processes can give rise to the observed gamma-ray variability, and we show below that the observations exhibit many features that are consistent with this model's consequences.

In Section 2, we review the theory of wakefield acceleration, and in Section 3, we review the gamma-ray emission processes relevant for the wakefield acceleration mechanism in the context of blazars. In Section 4, we detail our gamma-ray analysis set-up, and present our results in Section 5. We conclude in Section 6.

2 MAGNETOROTATIONAL INSTABILITY AND WAKEFIELD ACCELERATION

As a theory for the underlying electron energy injection, ponderomotive acceleration, a version of wakefield acceleration (Tajima & Dawson 1979), provides a theoretical framework of the extremely relativistic collective acceleration mechanism in an idealized case (Ebisuzaki & Tajima 2014a,b). In this mechanism, the wave front is regarded as one-dimensional only depending on the coordinate in the direction of the Alfven shock – and its mode-converted EM – waves along the jet propagation. In this one-dimensional model the coherence of high energy acceleration is guaranteed with the asymptotically tending velocity of the EM group velocity being the speed of light c (Tajima & Dawson 1979; Ashour-Abdalla et al. 1981). This is best realized when the pulse contains a single frequency carrier EM wave, just as is the case of a laboratory laser experiment. This may not be necessarily the case in our astrophysical setting, in which we expect a multiple set of frequencies of EM waves. However, we note that the group velocities of various EM waves with different frequencies are nearly equal to c in the one-dimensional case. Furthermore, as explained in the theory of Ebisuzaki & Tajima (2014a), the pulse is generated by the striking of an acceleration of matter ejected by a major disruption of the AGN accretion disc – the so-called magnetorotational instability (MRI). As such, an eruption could be represented by one major outburst (though could be a series of such) that results in a predominance of a single pulse with a typical length of the disc thickness. This results in the following situation: while the accelerating field acquires a complex phase structure, the phase velocity of each portion of the wave substructure is again close to c, i.e. $c\sqrt{(1-\omega_{\mathrm{p}}^2/\omega(z)^2)}$, where $\omega(z)$ is the frequency of that local, where z is along the jet propagation and substructure's frequency and ω_{p} is the plasma frequency where the pulse propagates. This mechanism is one of the origins of relativistic coherence, as pointed out in Tajima (2010).

The intense EM pulse is produced via collective (non-collisional) and coherent robust acceleration called the wakefield process (Tajima & Dawson 1979). This acceleration mechanism is via the ponderomotive force that is from the Lorentz term $q(v \times B)/c$. Suppose that the EM pulse is propagating in its axial (along the jet) direction (all it the z-direction) with the electric polarization of the EM pulse in the x-direction and the magnetic in the y-direction (circularly polarized case can be easily accommodated to the same effect). The rapidly oscillating EM fields cause a charged particle (such as an electron) to execute a figure-eight oscillatory orbit to relativistic velocities so that $v \sim c$ in the x-direction by this electric field E. Meanwhile, the magnetic field B in the y-direction causes this particle accelerated in the z-direction (longitudinal direction, the same as the EM pulse propagation) via the $v \times B$ force, which is called the ponderomotive force (Tajima 1985). In less extreme laboratory cases the ponderomotive force is often calculated by considering the envelope of the EM pulse (Sprangle & Esarey 1988). However, in our present ultrarelativistic regime [we define this as $qE/m\omega c = a_0 \gg 1$, where E is the electric field of the EM pulse, m the mass of the electron, ω the frequency of the EM (and Alfven) wave, and a_0 the normalized vector potential of the EM pulse (the strength parameter of the EM wave)], the ponderomotive force need not to be averaged over the pulse length, but rather its raw Lorentz force may directly impact acceleration in the longitudinal direction. Thus, noting that the magnetic field $B \sim E$, in the present underdense jet region (Ebisuzaki & Tajima 2014a), and $v_y \sim c$, we obtain the strength of the ponderomotive force $F_{\rm p}$ along the longitudinal direction is $F_{\rm p} = mc\omega a_0$. This ponderomotive force causes charge separation and triggers large plasma wave in the longitudinal direction with the accelerating field of $E_{\rm TD} = mc\omega_{\rm p}a_0/e$. The field is called the Tajima–Dawson field that is characteristic accelerating field of the wakefield acceleration (Tajima & Dawson 1979), where e is the electron charge and $\omega_{\rm p}$ is the plasma frequency. The plasma oscillations thus excited having the phase velocity of speed of light c are so far out of the plasma electron thermal velocity $v_{\rm th}$ that the plasma's disturbance is known to not have a disturbing influence on the wakefields. In addition, since in our case the EM pulse is in the ultrarelativistic regime, there is another mechanism to stabilize the wakefields. This is because in the ultrarelativistic regime the relativistic coherence plays additional role to stabilize the acceleration process (Tajima 2010). If the jet is flowing with a relativistic Lorentz factor Γ, the ponderomotive force becomes $F_{\rm p} = \Gamma mc\omega a_0$.

While the relativistic coherence is preserved in the one-dimensional situation, the escape of particles in this multifrequency EM drive becomes much more frequent than that of a single carrier case. This incessant detrapping (and subsequent retrapping and its repetition of these processes) gives rise to the emergence of phase-induced stochasticity (Mima et al. 1991). According to this theory, the resultant energy spectrum in one dimension takes E^{-2}, i.e. the energy spectral index of 2. That is, in the most ideal situation of purely one-dimensional ponderomotive acceleration, the energy spectrum takes index of 2. In less idealistic cases of two dimensions (or three dimensions), the ponderomotive acceleration incurred by waves that point to various directions (albeit within a narrow cone around the jet direction z) now makes the detrapping more rapid so that the accelerating length per one episode of the wave trapping of particles becomes shortened and the energy gain less. We call this as the shortening of the dephasing length as a function of the dimensions of the wave structure (Tajima & Dawson 1979). This leads to an energy spectral index greater than 2, with more particles dominating in lower energy bracket. If we compare the first one-dimensional case with the two-dimensional (three-dimensional) case, the amount of energy gain is higher in one dimension than in two dimensions, as more coherent energy gain is realized in the former. Thus, it is this intrinsic mechanism of the ponderomotive acceleration that makes the lower index case acquire greater and more coherent energy gain in one-dimensional than the cases in more spread wave propagation in two-dimensional (and three-dimensional) cases. Therefore, in ponderomotive acceleration, the energy spectral index naturally anticorrelates with the particle energy gain (and therefore the luminosity when converted into gamma-rays).

On the other hand, the recent wakefield acceleration mechanism (Ebisuzaki & Tajima 2014a) has been suggested of the genesis of highest energy cosmic rays accelerated via wakefields generated by the Alfven shock emanated from the jet from an AGN accretion disc disruptions. It has an embedded feature of accelerating both protons (ions) and electrons simultaneously. Moreover, it has built-in characteristics of the following: while the Fermi mechanism is fundamentally stochastic (Fermi 1954), the current mechanism is based on the coherent baseline process with the relativistic coherence, though there are elements that bring in stochastic processes that overlay the coherent mechanism. High-energy electrons accelerated by this mechanism in its purest form (dominated by nearly one-dimensional collimation along the axis of the blazar) have the power-law spectrum of energy with photon index of 2. If there are less ideal or less robust regime of its operation, the power index would rise above 2. When the wakefield generation is most robust, naturally the luminosity is also highest. The acceleration process has inherent rapid time-scales. The shortest time variation is about 100 s, reflecting the Alfven wave structure, the next time hierarchy has days–weeks associated with the occurrence of the accretion disruption interval, and the longest time-scale corresponds to the acceleration time of the highest energy cosmic rays (1–10^3 yr). This last time-scale is primarily for protons. For electrons with much lighter mass, the acceleration time-scale may be in the range from 100 s to weeks, in other words, the first and second time-scales, though the time structure depends on the detailed acceleration configuration. Although the gamma-ray luminosity integrated over 4π is on the order of 10^{41} erg s^{-1} for a black hole of 10^8 M$_\odot$ and normalized accretion rate of 0.1 M$_\odot$ yr^{-1}, the boosted-apparent luminosity reaches 10^{44}–10^{45} erg s^{-1}, depending on the γ-factor of the jet. This is within a few orders of magnitude of the observed gamma-ray luminosities of blazars. For example, blazar 3C 454.3 has a bolometric luminosity from 0.1 to 100 GeV of 4.1×10^{48} erg s^{-1} (Nolan et al. 2012). The episodic dynamics of the magnetic eruption of a black hole's accretion disc, along with the associated intense disruption of their jets, was studied via three-dimensional general relativistic magnetohydrodynamics in Mizuta et al. (2018).

We give a flowchart time-scale of the flux variation as connected between our MRI model and our observations in Fig. 1. The accretion of plasma amounts to intense excitation of pulsed Alfven shocks at the feet of the jets. A diagram of this mechanism is shown in fig. 1 of Ebisuzaki & Tajima (2014b). These shock waves propagate along the jets, turning themselves into EM pulses of super high intensity, as the plasma density in the jet makes the Alfven wave converting itself into EM pulse with phase velocity at speed of light c. The likely intensity of these pulses that are characterized by the normalized vector potential, $a_0 = eE_0/mcw_0$, where E_0 and w_0 are the EM pulse's amplitude and frequency, of the EM pulses are far beyond unity. Such intensity is termed as 'relativistically intense' pulses, as the EM acceleration of particles reach to relativistic momentum in a single period of its EM pulse. These relativistically intense (coherent) EM pulses are known to produce intense longitudinal (i.e. in the direction of the EM pulse propagation, not transverse to that direction) acceleration of charged particles (both electrons in its negative phase and positrons and protons in its positive phase) via the ponderomotive potential of these intense EM pulses. This acceleration process has been known and called as wakefield acceleration (Tajima & Dawson 1979) and its energy gain $E_{\rm acc}$ is theoretically and experimentally well known

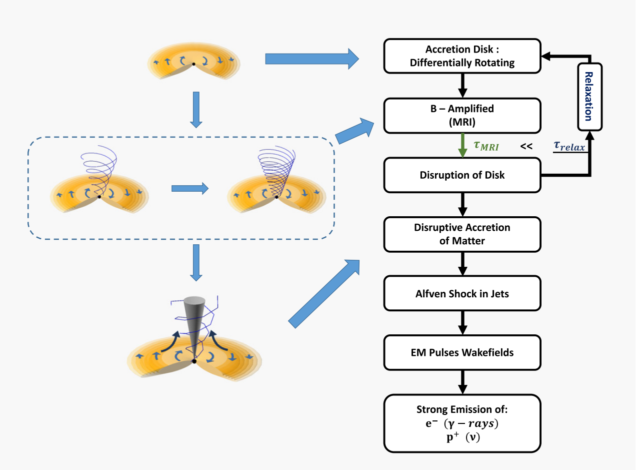

Figure 1. The accretion disc that contains embedded magnetic fields does two effects: (1) it will stretch the embedded magnetic fields by the differential rotation of the accretion disc, which tends to amplify the magnetic fields; (2) Such growth of magnetic fields and the differential rotation lead to the MRI (Balbus & Hawley 1991). The MRI-triggered disc instability leads to the accretion of concentrations of matter toward the centre of the disc and therefore the black hole. These concentrations of accreting matter should run into the feet emanating magnetic fields and jets out of the central black hole. These collisions of the plasma concentrations into the feet of the jets will disturb the jets' base. Once the magnetic fields give rise to the burst of matter to accrete, the magnetic fields leave the disc and relax to the state in which little magnetic fields in the disc. The disc repeats this pattern, as shown in the flowchart.

as $E_{\mathrm{acc}} = mc^2 a_0^2 n_{\mathrm{cr}}/n$, where the quantities n and n_{cr} are the plasma density and the critical density (Tajima, Nakajima & Mourou 2017).

Because of the genesis of the intense accelerating field generated by the above process characterized by the parameter a_0 (which can be looked upon as the relativistic Lorentz factor of the EM pulse), we understand that whenever the MRI is incurred in the disc, the accretion of plasma concentrations towards the black hole happens, MRI triggers the above pulse generation in the jets, and thereby both electrons and positively charged particles accelerated by the above intense pulse are emitted synchronously right after this accretion event. Because the MRI is episodically excited (Fig. 1), the emission of electron acceleration and ions is also excited, the former of which may be observed as increases in gamma-ray flux, while high-energy protons (and perhaps neutrinos) may also be emanated. We show this episodic flux and time-scale relationship, and its relation to our observations, in Fig. 2. As we discuss above, the higher flux periods are correlated with higher electron spectral index, but that is modulated by the synchrotron self-Compton model, as discussed below.

The theoretical prediction also indicates that the larger the central mass of the black hole is, the longer the repetitive recursion period of the MRI. Therefore, in future work, one can assess the mass of the central black hole from the repetitive period observed by the gamma-rays.

3 SYNCHROTRON TO INVERSE COMPTON ACCELERATION

In this section, we briefly review how accelerated electrons lead to the observed gamma-ray spectrum. For the majority of blazars the gamma-ray emission can be well described by the process of synchrotron self-Compton (Longair 2011). This is the process by which synchrotron photons, produced in great abundance by high-energy electrons in the magnetic field of the blazar jet, are up-scattered by inverse Compton collisions by these same electrons. Photons emitted by the accretion disc may also be up-scattered. The intensity spectrum has a characteristic double-humped feature where the high-energy gamma-ray emission is an inverse Compton processed up-scattering reflection of the lower energy emission (Fossati et al. 1997, 1998; Donato et al. 2001). A model spectrum of this variety is shown in Fig. 3. Here we review the basic physics of the synchrotron mechanism that feeds into the synchrotron self-Compton process, based on Longair (2011). The high-energy

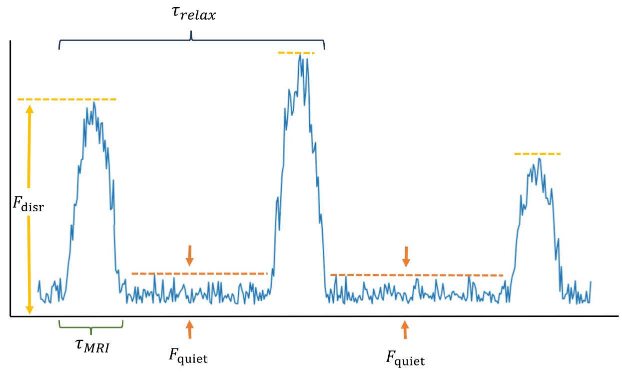

Figure 2. This is a cartoon depiction of the MRI instability versus relaxation time-scale. The MRI excitation time-scale is τ_{MRI}, originally calculated by Balbus & Hawley (1991), and the relaxation and spin-up scale time-scale τ_{relax} is given by Ebisuzaki & Tajima (2014b) to be $\tau_{\mathrm{relax}} \sim 10\tau_{\mathrm{MRI}}$. The lower flux level ($F_{\mathrm{quiet}}$) is the quiet phase flux as given by such theory as in Blandford & Znajek (1977), while the high flux phase (F_{disr}) is given by the disruptive accretion phase such as by Mizuta et al. (2018).

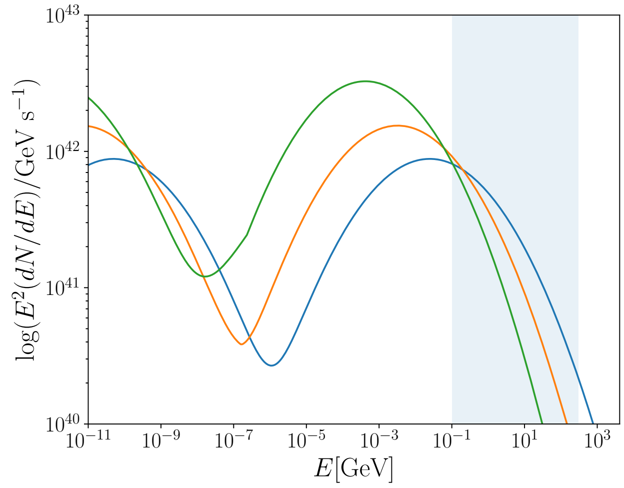

Figure 3. Shown is a standard blazar sequence model for a typical blazar SED, based on Inoue & Totani (2009). The energy band of our observations is indicated by the filled blue box. As can be seen in this illustration, a higher luminosity (green curve), relative to a lower luminosity (blue curve), would correspond to a photon spectral index much steeper than $\Gamma = 2$ within the observational window. This is what we dub the 'internal blazar sequence.' A spectral index of $\Gamma = 2$ is horizontal on this plot. The orange curve represents the possibility of observing the photon spectrum that is more closely tied to the intrinsic electron spectrum at higher energies than the inverse Compton peak intensity.

gamma-ray spectrum of blazars may also have contributions from high-energy hadronic cosmic rays (Takami, Murase & Dermer 2013), though synchrotron self-Compton models in general do a superior job in explaining the broad blazar SED.

The primary energy flux at a given frequency ν, $J(\nu)$, peaks in synchrotron emission at a characteristic frequency,

$$\nu_c \approx \gamma^2 \nu_g = \left(\frac{E^2}{m_e c^2}\right)^2 \nu_g, \tag{1}$$

for an electron of energy E, where the gyrofrequency is $\nu_g = eB/2\pi m_e$. The energy radiated in frequency interval $(\nu, \nu + d\nu)$ is

$$J(\nu)\,d\nu = \left(-\frac{dE}{dt}\right) N(E)\,dE, \tag{2}$$

where the electron population has a number distribution as $N(E)dE = \kappa E^{-p}dE$. The energy-loss rate for synchrotron radiation is

$$-\left(\frac{dE}{dt}\right) = \frac{4}{3}\sigma_T c \left(\frac{E}{m_e c^2}\right)^2 \frac{B^2}{2\mu_0}, \tag{3}$$

and the energy flux is

$$J(\nu) \propto \kappa B^{(p+1)/2} \nu^{-(p-1)/2}. \tag{4}$$

So, the emitted synchrotron spectrum $J(\nu) \propto \nu^{-a}$ is related to the intrinsic electron energy spectrum p as $a = (p - 1)/2$. However, the synchrotron emission undergoes self-absorption that alters the observed spectrum. This is due to the limitation that no region can emit incoherent radiation at an intensity greater than that of a blackbody at its thermodynamic temperature. At low enough frequencies, the 'brightness temperature' of the radiation approaches the 'thermal' temperature of the radiating electrons. The *brightness temperature* is derived from that of a blackbody, but is applicable to any emission process, and is defined as $T_b = (\lambda^2/2k)(S_\nu/\Omega)$, where λ is the emission wavelength, S_ν is the flux density, and Ω is the solid angle the source subtends at the observer. The effective temperature of the electrons must match the brightness temperature, and therefore the observed intensity must be (Longair 2011)

$$S_\nu \propto \frac{\nu^{5/2}}{B^{1/2}}. \tag{5}$$

Therefore, a pure synchrotron self-absorption spectrum is a rising spectrum as $I \propto \nu^{5/2}$ and then falls over to the inherent synchrotron spectrum $I \propto \nu^{-(p-1)/2}$. The inverse Compton spectrum reflects that since in that case the energy of the up-scattered photons is $\hbar\nu = (4/3)\gamma^2\hbar\nu_0$, where ν_0 is the originating photon's frequency.

There is one basic conclusion regarding the relation of the observed photon spectrum in gamma-rays or radio frequencies: the observed energy spectrum could reflect the originating spectrum well above the synchrotron peak where $I_\nu \propto \nu^{-(p-1)/2}$, but that is not necessarily achieved in the given observational window, which could lie below the synchrotron peak, near it, or above it, but still in its spectrally curved region.

For an example blazar temporal sequence, we adopt the SED spectral model first quantified in Inoue & Totani (2009). However, any smoothly curved spectrum is likely sufficient, and we make no effort to fit a model. We show for the first time that, for the case of low synchrotron peak blazars we observe, the temporal variation of flux is consistent with a given blazar shifting in flux and bolometric luminosity along such a temporal blazar sequence. Our results of observed gamma-ray spectra appear to be near the intensity peak (overturn) of the inverse Compton emission, where $a = 2$, and so are not likely reflective of the source electron spectra. Higher energy observations, such as with the High Altitude Water Cherenkov (HAWC) gamma-ray observatory (Lauer & Younk 2015), MAGIC (Aleksic et al. 2012), H.E.S.S. (Hinton 2004), and, eventually, the Cherenkov Telescope Array (CTA; Cherenkov Telescope Array Consortium 2019), as well as temporal observations, may say more about the intrinsic electron spectra. The cutoff shape could also be due to the emergence of an upper electron energy for inverse Compton emission, and that would have to be taken into account in modelling of the highest energy spectra in future work (Lefa, Kelner & Aharonian 2012).

In summary, our observations could connect the temporal properties of the wakefield acceleration mechanism, but a connection with the intrinsic electron spectra is not possible with the lower energy *Fermi*-LAT spectra. Importantly, the high-energy spectra will be modified by intergalactic opacity, which becomes significant for gamma-ray energies of more than 10–100 GeV (Abdo et al. 2010e). Therefore, any deconvolution of the electron energies from the photon spectrum at high energies will have to take into account effects of attenuation of gamma-rays as well for the blazar observed (Gilmore et al. 2012).

4 METHOD

Throughout our analysis, we use FERMITOOLSversion v9r33p0 to study *Fermi*-LAT Pass 7 reprocessed data taken from 2008 August to 2015 February (approximately 85 months of data), using both front- and back-converting SOURCE class photons. We select the 12 blazars with the highest photon flux from the *Fermi*-LAT second AGN catalogue (Ackermann et al. 2011). (Note that the analysis does depend on the Pass version of the data.) These blazars are listed in Table 1, along with their optical and SED class. For each blazar, gamma-rays within a circular region of interest (ROI), 7° in radius and centred on the blazar, are selected, as was done in Abdo et al. (2010a). We use photons with energies between 100 MeV and 300 GeV, and apply the standard cuts recommended by the *Fermi* Collaboration to ensure data quality (zenith angle $< 100^\circ$, DATA_QUAL = 1, LAT_CONFIG = 1).

Our model for each of the 12 ROIs is composed of all of the sources identified in the LAT 4-year Point Source Catalog (3FGL), along with the recommended diffuse emission models associated with the Galactic emission (GLL_IEM_V05_REV1) and the isotropic background (ISO_SOURCE_V05) that account for the contributions from both the extragalactic background and cosmic ray contamination. Despite the fact that a number of blazars in this analysis display curvature in their spectra over wide ranges in energy, we employ an energy window where the curvature is minimal and well modelled by a power law. We adopt simple power-law model consisting of two free parameters, a normalization factor N_0 and spectral index Γ, for the spectrum of each blazar. The convention used in this paper is that the spectral index Γ should be taken to be positive, so that the photon flux is proportional to $E^{-\Gamma}$, where E is the energy. This is done to provide a convenient means of characterizing the relative hardness or softness of the photon spectrum, which is the primary goal of this analysis.

Once we construct a model for the ROI around a particular blazar, we use standard maximum likelihood methods to fit the free parameters of the various gamma-ray sources in our model. To determine which parameters to vary, we make use of the quantity TS, which is defined as twice the difference in log-likelihood between a model with and without a particular source, i.e. $\mathrm{TS} = 2\Delta\ln(\mathcal{L})$ (TS = 25 corresponds to an approximate detection significance of

Table 1. List of blazars and their properties, sorted in order of decreasing photon flux, with their Pearson correlation coefficient between their photon flux and spectral index, along with the corresponding approximate *p*-value for the 50 time bins analysis.

Blazar name	Optical class	SED class	r	p-value	$\sigma^2_{\mathrm{NXS,flux}}$	$\sigma^2_{\mathrm{NXS,index}} \times 10^{-2}$
3C 454.3	FSRQ	LSP	− 0.416	2.7×10^{-3}	2.44 ± 0.010	1.44 ± 0.14
PKS 1510−08	FSRQ	LSP	− 0.441	1.3×10^{-3}	0.99 ± 0.012	0.04 ± 0.03
PKS 1502+106	FSRQ	LSP	− 0.681	5.1×10^{-8}	1.306 ± 0.026	0.42 ± 0.40
PKS 0537−441	BL Lac	LSP	−0.379	6.7×10^{-3}	0.381 ± 0.013	0.38 ± 0.09
4C +21.35	FSRQ	LSP	− 0.491	3.0×10^{-4}	1.28 ± 0.017	0.68 ± 0.12
PKS 0426−380	BL Lac	LSP	− 0.254	7.5×10^{-2}	0.34 ± 0.013	0.50 ± 0.10
Mrk 421	BL Lac	HSP	− 0.065	6.5×10^{-1}	0.165 ± 0.008	0.03 ± 0.03
3C 279	FSRQ	LSP	− 0.265	6.3×10^{-2}	0.82 ± 0.016	0.23 ± 0.07
3C 66A	BL Lac	ISP	0.104	4.7×10^{-1}	0.21 ± 0.016	1.49 ± 0.04
PKS 2155−304	BL Lac	HSP	0.680	5.6×10^{-8}	0.40 ± 0.023	0.52 ± 0.12
PKS 0454−234	FSRQ	–	−0.587	7.4×10^{-6}	0.34 ± 0.013	0.49 ± 0.12
PKS 0727−11	FSRQ	–	− 0.145	3.1×10^{-1}	0.31 ± 0.019	1.20 ± 0.28

about 5σ for point sources). We then determine the variability of the photon flux and spectral index over time for each of the 12 blazars by dividing up the full time range into time bins and refitting the parameters for the source of interest, leaving all other sources in the ROI fixed to their best-fitting values found from the full time range. Because the blazar is, by a large factor, the brightest source in the ROI for all cases, any variability of other sources is minimal and would not alter our results. Our procedure, which makes use of the LAT analysis scripts QUICKANALYSIS, QUICKLIKE, and QUICKCURVE, is described in more detail below.

(i) First, a binned likelihood analysis of the region is performed using photons from the full time range. This is referred to as the DC analysis (analogous to ‘direct current’).

(a) The raw photons file is filtered and processed according to the previously described specifications for each blazar using the QUICKANALYSIS tool.

(b) The model file for the ROI is generated using the user contributed tool MAKE3FGLXML.PY and then changing the spectral shape of the source of interest to a power law.

(c) The parameters for sources with TS > 25 are left free. Sources with $4 <$ TS < 25 have their spectrum fixed to their 3FGL values but their normalizations are left free. Finally, sources with TS < 4 have all of their parameters fixed to their 3FGL values.

(d) A standard binned maximum likelihood analysis is performed using the QUICKCURVE tool to find the best-fitting values for all of the remaining free parameters in the model. This model is called the DC model.

(ii) Next, the full time range is divided up into time bins and a separate unbinned likelihood analysis is performed for each time bin. This is referred to as the AC analysis (analogous to ‘alternating current’).

(a) The entire time range is divided into equally sized time bins of 7.9 d, resulting in a total of 300 time bins. Though there may be temporal variation on time-scales smaller than this, our timing resolution is limited by the detection significance of the source of interest, and we are unable to reliably probe time-scales significantly shorter than about a week.

(b) All of the relevant analysis files to perform an unbinned likelihood analysis for each time bin are generated using the QUICKCURVE tool, using the same specifications as in step (i).

(c) The DC model from step (i) is copied, but all of the sources except for the source of interest are fixed to their best-fitting values from the DC analysis. Only the normalization factor and spectral index of the source of interest are left free.

(d) An unbinned maximum likelihood analysis is performed in order to determine the best-fitting values for the normalization and spectral index of the source of interest.

(iii) Step (ii) is repeated once again, but using time bins that are larger by a factor of 6 (about 47.5 d), resulting in 50 time bins instead of 300. This has the effect of increasing the detection significance of the source of interest in each time bin at the cost of losing sensitivity to short time-scale variations.

5 RESULTS

We find that all blazars displayed significant temporal variation in both their flux and spectral index. Fig. 4 shows the variation of the flux and spectral index for blazar 3C 454.3 over the 300 time bins. For nine out of the 12 blazars studied in this analysis, we observe a weak to moderate anticorrelation between the flux of the blazar and its spectral index. Six of these are statistically significant (p-value < 0.05). In other words, for most of the blazars, we observe the same ‘harder when brighter’ effect that has been noted in other analyses (Abdo et al. 2010a). This can be seen in Fig. 4, as the peaks in flux correspond to dips in the spectral index and vice versa.

This anticorrelation can be seen more clearly in Fig. 5 that shows the spectral index versus flux for nine of the blazars in the 50 time bins analysis. The anticorrelation is seen in both the 50 time bins analysis and the 300 time bins analysis. The Pearson correlation coefficients are shown in Table 1 along with their corresponding approximate p-values. Three blazars do not exhibit this anticorrelation (Fig. 6). Two of the three, Mrk 421 and PKS 2155−304, are high synchrotron peak (HSP) BL Lacertae objects (BL Lacs), and the third blazar, 3C 66A, is an intermediate synchrotron peak (ISP) BL Lac. This same pattern of flat-spectrum radio quasars (FSRQs) and low synchrotron peak (LSP) BL Lacs displaying the anticorrelation and HSP BL Lacs not exhibiting the effect was previously noted in Abdo et al. (2010a), although they also note that ISP BL Lacs tend to display it in some cases. Possible explanations for this behaviour will be elaborated on further in Section 6.

We estimate the intrinsic source variance by calculating the excess variance σ^2_{XS}, as described in Vaughan et al. (2003). The excess variance is the variance after subtracting the contribution from measurement errors such as Poisson noise and is defined as

$$\sigma^2_{\mathrm{XS}} = S^2 - \overline{\sigma^2_{\mathrm{err}}}, \tag{6}$$

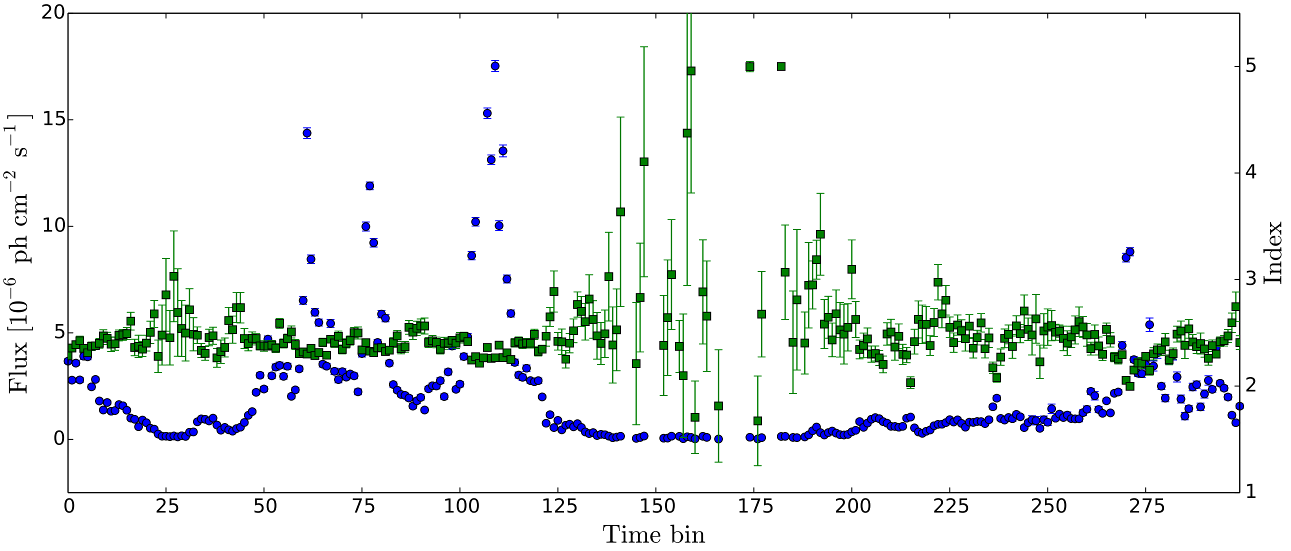

Figure 4. Shown are the flux (blue circles, left-hand axis) and spectral index (green squares, right-hand axis) for 3C 454.3 in 300 time bins of 7.9 d duration. An anticorrelation can be seen: the peaks in flux correspond to dips in the spectral index and vice versa.

where S^2 is the sample variance of N data points,

$$S^2 = \frac{1}{N-1}\sum_{i=2}^{N}(x_i - \overline{x})^2, \tag{7}$$

and $\overline{\sigma^2_{\rm err}}$ is the mean square error,

$$\overline{\sigma^2_{\rm err}} = \frac{1}{N}\sum_{i=1}^{N}\sigma^2_{{\rm err},i}. \tag{8}$$

The normalized excess variance is given by $\sigma^2_{\rm NXS} = \sigma^2_{\rm XS}/\overline{x}^2$, and the error on $\sigma^2_{\rm NXS}$ was calculated according to

$$\mathrm{err}(\sigma^2_{\rm NXS}) = \sqrt{\left(\sqrt{\frac{2}{N}}\,\frac{\overline{\sigma^2_{\rm err}}}{\overline{x}^2}\right)^2 + \left(\sqrt{\frac{\overline{\sigma^2_{\rm err}}}{N}}\,\frac{2F_{\rm var}}{\overline{x}}\right)^2}, \tag{9}$$

as given in Vaughan et al. (2003). Here, $F_{\rm var}$ is the fractional root mean square (rms) variability amplitude and is simply the square root of the normalized excess variance, i.e. $F_{\rm var} = \sqrt{\sigma^2_{\rm NXS}}$. The measured values for normalized excess variance of the photon flux $\sigma^2_{\rm NXS,flux}$ and for the spectral index $\sigma^2_{\rm NXS,index}$ are also shown in Table 1.

6 DISCUSSION

We have established the anticorrelation between the luminosity of gamma-rays from blazars and their spectral index. The anticorrelation is clearly consistent with a shift from off-peak to peak portions of the blazar spectra, as shown in Figs 3 and 5, for the case of LSP BL Lac blazars. This is the first time that a temporal-sequence model has been applied to show the origin of the spectral–flux anticorrelation.

We followed in this study the earlier observations by Abdo et al. (2010a,b). In our work, we scan different blazars with different values of flux and index, as in these prior analyses. When they surveyed different blazars, they showed different rise times of the brightening and the lowering of the spectral index and the interval times between such bursts of luminosity surge. The rise (and fall) times in most cases scale with the interval times between the events, i.e. the longer the rise time of the burst is, the longer the interval is. This is predicted in the MRI and wakefield acceleration model of Mizuta et al. (2018). Even though the time-scale varies over orders of magnitude, this phenomenon is universal. In fact, Ebisuzaki & Tajima (2014a) predict that all these events are universally based on the wakefield excitation in the jets sharing the common acceleration mechanism, which is the basis for this universality.

We note that the observed phenomenon of the anticorrelation between the luminosity and the spectral index remains manifest, regardless of the mentioned rise time and interval time-scales. According to the theory of Ebisuzaki & Tajima (2014a), the periods of both the rise time and the interval time-scale are proportional to the mass of the central AGN mass (Ebisuzaki & Tajima 2014a). In other words, though an AGN with different mass may show a proportional time-scale of variability, these phenomena are common and the luminosity–index anticorrelation is one of the strongest evidence for the universal nature of acceleration mechanism. It should be further noted that not only these universal phenomena are expected and/or observed in blazars, but also these should be expected for microquasars with much smaller masses, as predicted in Ebisuzaki & Tajima (2014b). Therefore, it is encompassing several orders of a wide range of masses from microquasars to most massive AGNs. From this discussion, we now suggest the following prediction: from the period time-scale of the blazar gamma-ray emissions, we can surmise the mass of the central object of the particular blazar. Therefore, the intrinsic luminosity of blazars, though collective of apparent luminosity depends on the observational conditions, can also tell us about the mass of the central object, as they also scale proportional to the mass (Ebisuzaki & Tajima 2014a,b).

Our own analysis (Fig. 4) and subsequent analyses also underline the following picture: when the gamma-ray emission from blazars increases, the gamma-ray spectrum tends to become harder. This observed tendency, which is in agreement with previous observation (Abdo et al. 2010a), is consistent with a temporal SED sequence, shifting emission from near-peak to peak inverse Compton emission flux. Higher energy observations, such as with the HAWC Observatory, may be able to probe the intrinsic electron spectrum to test

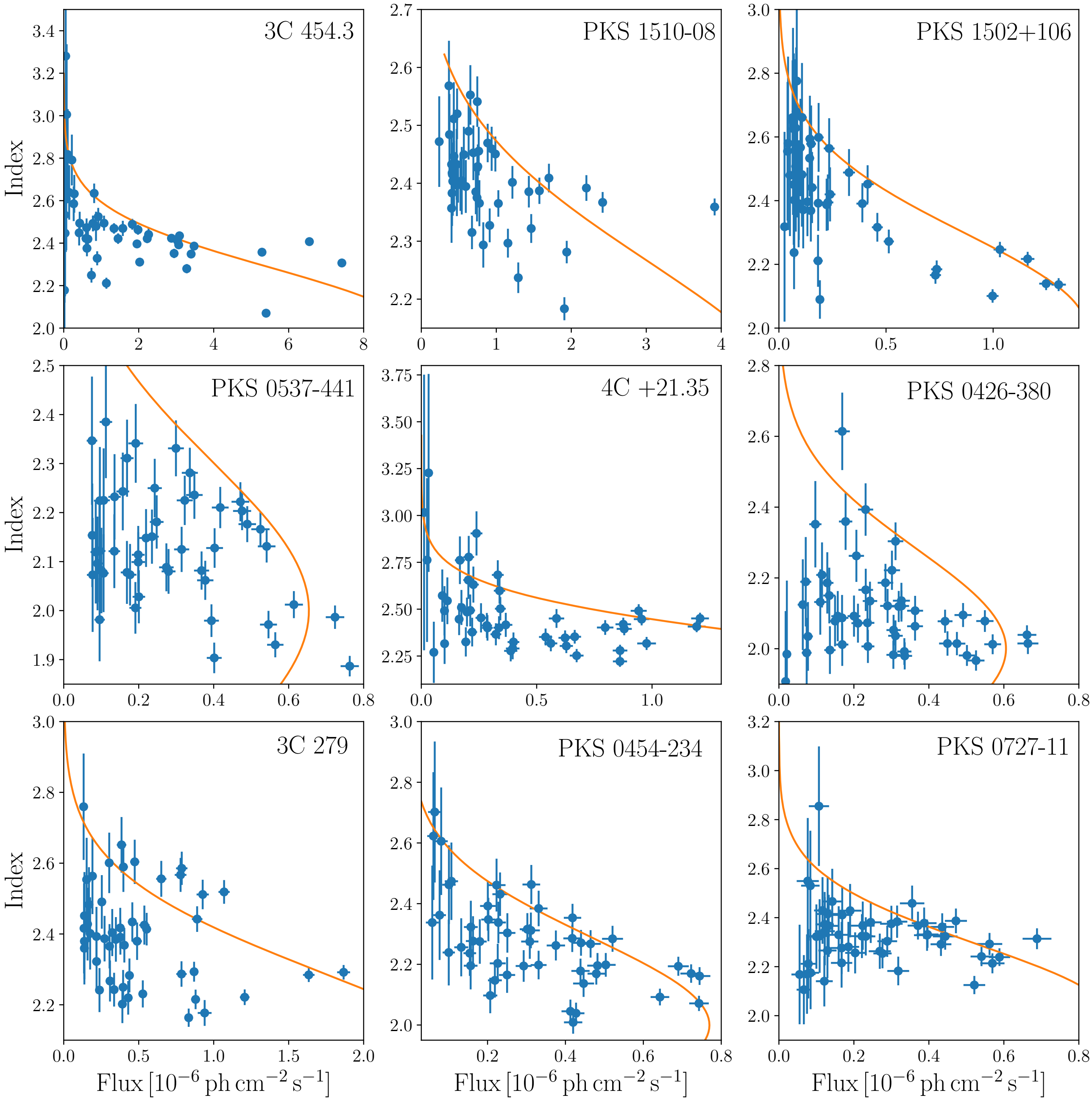

Figure 5. Shown here are the flux versus index for the nine blazars analysed in the 50 time bins analysis that exhibit the flux–spectral anticorrelation attributable to the inverse Compton up-scattering of synchrotron photons. The orange curve is the slope from the blazar SED model shown in Fig. 3, which is not fit to the data, yet corresponds well with the observations. This is what we dub the ‘internal blazar sequence’.

its consistency with the wakefield acceleration electron spectra in the jets. For HSP and ISP blazars, we do not see the anticorrelation as we had for LSP blazars with lower energy synchrotron peaks. This is due to the fact that, for HSP and ISP, the spectral peak is within the energy window not exhibiting the monotonic SED sequence anticorrelation. In addition, several of our tested HSP and ISP blazars exhibit no significant curvature in their spectra (Abdo et al. 2010c).

The episodic disc instability launches the energetic Alfven shocks, and their subsequent EM pulsations, such as in the Ebisuzaki–Tajima mode (Ebisuzaki & Tajima 2014a). This model naturally points to a localized source (as observed in Albert et al. 2007; Abdo et al. 2010a). Such localized emission of gamma-rays (arising from accelerated electrons) and expected localized acceleration of ions from such locations are integral properties of the wakefield acceleration mechanism. Furthermore, the wakefield acceleration of ultrahigh-energy cosmic ray ions has the unique property of localized gamma-ray emission, while the Fermi acceleration mechanism relies on a diffuse site and therein lies the difficult issue of stochastic genesis. In addition to the above issue of superhigh energetic genesis of cosmic rays (and associated variable gamma-ray emissions), the wakefield acceleration mechanism should be a natural candidate for more compact gamma-ray emission from e.g. Crab Nebula (Abdo et al. 2011; Buehler et al.

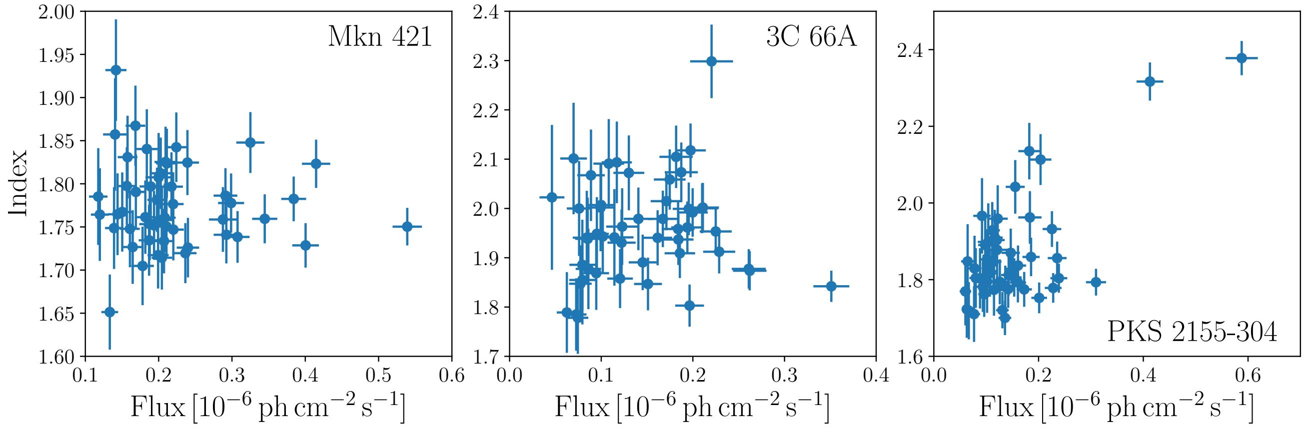

Figure 6. Shown here are the flux versus index for three blazars not exhibiting the flux–spectral index anticorrelation. Unlike the LSPs in Fig. 5, two of the three, Mrk 421 and PKS 2155−304, are HSP BL Lacertae objects (BL Lacs), and the third blazar, 3C 66A, is an ISP BL Lac. The pattern of FSRQs and LSP BL Lacs displaying the anticorrelation and HSP BL Lacs not exhibiting the effect was previously noted in Abdo et al. (2010a). ISP BL Lacs tend to display it in some cases. We discuss these differentiated cases in Section 6.

2012) and the microquasar Cygnus X-1 (Cyg X-1; Nowak et al. 2012; Ebisuzaki & Tajima 2014b). With continued observations of high-energy gamma-ray emission from blazars, especially those at the highest energies, the underlying emission processes and acceleration mechanisms may be further revealed.

ACKNOWLEDGEMENTS

NEC and KNA were supported in part by NSF Grants PHY-1316792, PHY-1620638, and PHY-1915005. TT has been supported by the Norman Rostoker Fund. We would like to acknowledge fruitful discussions with Aaron Barth.

REFERENCES

Abdo A. A. et al., 2010a, ApJ, 710, 1271
Abdo A. A. et al., 2010b, ApJ, 715, 429
Abdo A. A. et al., 2010c, ApJ, 716, 30
Abdo A. A. et al., 2010d, ApJ, 722, 520
Abdo A. A. et al., 2010e, ApJ, 723, 1082
Abdo A. A. et al., 2011, Science, 331, 739
Ackermann M. et al., 2011, ApJ, 743, 171
Aharonian F., 2007, ApJ, 664, L71
Albert J. et al., 2007, ApJ, 669, 862
Aleksic J. et al., 2011, ApJ, 730, L8
Aleksic J. et al., 2012, Astropart. Phys., 35, 435
Ashour-Abdalla M. et al., 1981, Phys. Rev. A, 23, 1906
Balbus S. A., Hawley J. F., 1991, ApJ, 376, 214
Blandford R. D., Znajek R. L., 1977, MNRAS, 179, 433
Buehler R. et al., 2012, ApJ, 749, 26
Chen L.-E., Li H.-Z., Yi T.-F., Zhou S.-B., Li K.-Y., 2013, Res. Astron. Astrophys., 13, 5
Cherenkov Telescope Array Consortium, 2019, Science with the Cherenkov Telescope Array. World Scientific Press, Singapore
Donato D., Ghisellini G., Tagliaferri G., Fossati G., 2001, A&A, 375, 739
Ebisuzaki T., Tajima T., 2014a, Astropart. Phys., 56, 9
Ebisuzaki T., Tajima T., 2014b, European Phys. J. Special Topics, 223, 1113
Edelson R., Mushotzky R., Vaughan S., Scargle J., Gandhi P., Malkan M., Baumgartner W., 2013, ApJ, 766, 16
Edelson R., Vaughan S., Malkan M., Kelly B., Smith K., Boyd P., Mushotzky R., 2014, ApJ, 795, 2
Fermi E., 1954, ApJ, 119, 1
Fossati G., Celotti A., Ghisellini G., Maraschi L., 1997, MNRAS, 289, 136
Fossati G., Maraschi L., Celotti A., Comastri A., Ghisellini G., 1998, MNRAS, 299, 433
Giannios D., Uzdensky D. A., Begelman M. C., 2009, MNRAS, 395, L29
Gilmore R. C., Somerville R. S., Primack J. R., Dominguez A., 2012, MNRAS, 422, 3189
Hinton J. A., 2004, New Astron. Rev., 48, 331
Inoue Y., Totani T., 2009, ApJ, 702, 523
Lauer R. J., Younk P. W., 2015, Presented at the 34th International Cosmic Ray Conference (ICRC2015), The Hague, The Netherlands, preprint (arXiv:1508.04479)
Lefa E., Kelner S. R., Aharonian F. A., 2012, ApJ, 753, 176
Longair M. S., 2011, High Energy Astrophysics. Cambridge Univ. Press, Cambridge
Marscher A. P. et al., 2008, Nature, 452, 966
Matsumoto R., Tajima T., 1995, ApJ, 445, 767
Mima K., Horton W., Tajima T., Hisegawa A., 1991, in Yoshikawa Y. H., Tajima T., eds, AIP Conf. Proc. Vol. 230, Nonlinear Dynamics and Particle Acceleration. Am. Inst. Phys., New York, p. 27
Mizuta A., Ebisuzaki T., Tajima T., Nagataki S., 2018, MNRAS, 479, 2534
Nolan P. L. et al., 2012, ApJS, 199, 31
Nowak M. A., Wilms J., Pottschmidt K., Markoff S., 2012, Mem. Soc. Astron. Ital., 83, 202
Sprangle P., Esarey E., 1988, Appl. Phys. Lett., 53, 2146
Tajima T., 1985, Laser Part. Beams, 3, 351
Tajima T., 2010, Proc. Jpn. Acad. Sci. B, 86, 147
Tajima T., Dawson J. M., 1979, Phys. Rev. Lett., 43, 267
Tajima T., Shibata K., 2002, Plasma Astrophysics. Perseus, Cambridge, MA
Tajima T., Nakajima K., Mourou G., 2017, Rivista Nuovo Cimento, 40, 33
Takami H., Murase K., Dermer C. D., 2013, ApJ, 771, L32
Tavecchio F., Roncadelli M., Galanti G., Bonnoli G., 2012, Phys. Rev. D, 86, 085036
Vaughan S., Edelson R., Warwick R. S., Uttley P., 2003, MNRAS, 345, 1271

This paper has been typeset from a TEX/LATEX file prepared by the author.